



## Convective dropwise condensation heat transfer in mini-channels with biphilic surface

Jindou Yuan<sup>a</sup>, Yanbo Wang<sup>a</sup>, Jinliang Xu<sup>a,b,\*</sup>, Xianbing Ji<sup>a</sup>, Jian Xie<sup>a,\*</sup>

<sup>a</sup>The Beijing Key Laboratory of Multiphase Flow and Heat Transfer, North China Electric Power University, Beijing 102206, China

<sup>b</sup>Key Laboratory of Condition Monitoring and Control for Power Plant Equipment of Ministry of Education, North China Electric Power University, Beijing 102206, China

### ARTICLE INFO

#### Article history:

Received 4 October 2018

Received in revised form 3 January 2019

Accepted 4 January 2019

Available online 11 January 2019

#### Keywords:

Dropwise condensation

Biphilic surface

Wettability

Droplet dynamics

Fluid mechanics

### ABSTRACT

For dropwise condensation (DWC) in confined channels, droplets slide on surface and may spoil the nano-pillars, thus the nano-pillars structure is not suitable. Here, we provide a robust biphilic surface with polymer film as hydrophobic wettability. Mesh screen is sintered on copper surface to form welding junction array. Dipping the sintered package in a Teflon solution followed by baking technique forms a hydrophobic coating film. Hydrophilic dots are exposed by separating mesh screen from copper substrate. Condensation experiment was performed in a mini-channel with dimensions of  $30.0 \times 3.13 \times 0.97 \text{ mm}^3$  and pure water–vapor as the working fluid. Mass flux covered a range of 10.5–63.8  $\text{kg/m}^2 \text{ s}$ . It is shown that condensation heat transfer coefficients on biphilic surface were 5.54 times of those on polished copper surface, and 1.89 times of those on hydrophobic polymer layer surface, maximally. Pressure drops are almost identical in condensers with biphilic surface and hydrophobic surface. For DWC on biphilic surface, growing droplet on hydrophilic dot attracts and merges neighboring droplets to generate *directional-droplets-coalescence*, explained by the Gibbs energy analysis. Higher droplet departure frequency was observed on biphilic surface than hydrophobic surface. Compared with hydrophobic surface, droplet on biphilic surface has different contact angle, covers several hydrophilic dots and reduces droplet thermal resistance. The above effects explain the heat transfer enhancement mechanism when biphilic surface is present.

© 2019 Elsevier Ltd. All rights reserved.

### 1. Introduction

The performance of a condenser plays an important role to influence the overall performance of an energy conversion or management system. For example, a Rankine cycle needs a condenser to complete vapor–liquid phase change for power generation. The condenser performance influences temperature/pressure distribution along the cycle to determine the cycle efficiency [1]. Atmospheric water, especially fog, represents a significant but largely untapped fresh water source, especially in semi-arid regions, desert regions, land-scarce regions with high economic activities. Recent progress has been made to condense water drops from air environment for human survival [2,3]. In electronic industry, high heat fluxes should be dissipated by an efficient cooling device such as heat pipe. A condenser condenses and returns liquid to an evaporator to operate a heat pipe [4].

Schmidt et al. [5] found dropwise condensation (DWC) on a chrome plated copper surface in 1930. Heat transfer coefficient of DWC is several times of filmwise condensation (FWC). Early DWC studies were performed on gold/silver surface, which attracts and deposits organic substances to account for heat transfer enhancement [6]. Because gold or silver is expensive, later investigators coated organic substance on metal surface by self-organization or ion-implanted technique [7].

Recently, various super-hydrophobic nanostructure surfaces have been developed to improve the DWC. These surfaces provide large contact angle and low contact angle hysteresis, ensuring easy droplet detachment [8]. Especially, the coalescence-induced-jumping promotes droplets departure [9]. Nanostructure surface does not always enhance heat transfer [10–12]. Xie et al. [13] developed a theoretical model for DWC on nanostructure surface. The contact angles were treated to show correct trend with respect to Cassie, partial Wenzel and Wenzel morphologies. A mixed droplet detachment model was developed to consider coalescence-induced-jumping, rolling and sliding modes, simultaneously. They concluded the DWC as an outcome of a series of positive and negative effects by introducing nanostructure. The increased droplet

\* Corresponding authors at: The Beijing Key Laboratory of Multiphase Flow and Heat Transfer, North China Electric Power University, Beijing 102206, China (J. Xu).  
E-mail addresses: [xjl@ncepu.edu.cn](mailto:xjl@ncepu.edu.cn) (J. Xu), [xiejian90@ncepu.edu.cn](mailto:xiejian90@ncepu.edu.cn) (J. Xie).

population density and number of drop nucleation sites are positive contributions, while the decreased heat transfer rate of single drop and additional nano-porous thermal resistance are negative contributions. Besides, the long-time-operation of DWC may cause nanostructure failure to deteriorate heat transfer [14].

A DWC cycle consists of drop nucleation, growth, coalescence and detachment [15]. To achieve better DWC performance, different wettabilities are demanded. Hydrophilic surface has high energy to promote drop nucleation. Alternatively, hydrophobic surface has low energy to repel droplets. To overcome this contradiction, a mixed wettability surface with hydrophilic islands/cavities populated on hydrophobic surface has been tried by many authors [16–23]. The studies were performed in humid air environment or in pool vapor condensation condition.

Under many circumstances, DWC takes place in a confined space. For example, a printed circuit heat exchanger has a  $\sim$ mm scale channel height [24]. A miniature heat pipe requires an efficient condenser in which DWC occurs in a confined space [4]. Convective dropwise condensation in a confined space introduces new problems. The bulk phenomenon is important for condensation in large space, but the wall effect plays important role in small channels [25]. The 3D effects are apparently decreased in narrow channels. The capillary length is  $l_c = \sqrt{\sigma/(g\Delta\rho)}$ , where  $\sigma$  is surface tension,  $g$  is gravity acceleration, and  $\Delta\rho$  is density difference between liquid and vapor. For water-vapor system,  $l_c$  is  $\sim$ 2.5 mm. The droplet confinement number,  $Co$ , is defined as the ratio of capillary length  $l_c$  to channel characteristic size such as channel height  $\delta$ , written as  $Co = l_c/\delta$ . When channel height is down to  $\sim$ mm scale,  $Co$  is large than 1 to yield droplet confinement, altering droplet departure mode. Usually, droplets are confined in channel height direction to form cake shape to have a largest possibility to slide along flow direction, whereas condensation in large space creates fruitful departure modes such as jumping, rolling and sliding [13]. Imagining droplets in a confined channel formed by two super-hydrophobic walls, for 10–100  $\mu$ m droplets which are smaller than channel height, the coalescence-induced-jumping can be repeated several times to merge more tiny droplets, until a large droplet thoroughly occupies the channel height.

Droplets shall travel a long distance to reach channel outlet, and nano-pillars (nano-grass, nano-needle, nano-wire) surface will be spoiled [26]. The possible failure mechanisms are described here. First, if a local nano-pillars region is periodically flushed by droplets, nano-pillars will fall down, which is similar to *stone rolls on the lawn to spoil the grasses*. Second, when a droplet slides on a hydrophobic surface, nano-pillars near contact line receive ultra-large stress, due to ultra-large pressure difference across liquid region and vapor region. Thus, the nano-pillars structure may be useful for DWC in large space, but it has distinct drawback to resist nanostructure failure for DWC in confined space.

Few studies were reported on condensation in confined channels. Chen et al. [27] found droplet nucleation, growth, coalescence and flushing in hydrophobic channels. When the vapor velocity increases, droplets departure diameter becomes smaller and the droplet flushing frequency increases to enhance heat transfer. Fang et al. [28] studied condensation in silicon-microchannels having three droplet contact angles of 25°, 91° and 123°. Flow pattern, heat transfer and pressure drop were found to be influenced by surface wettabilities. The hydrophobic channel had higher heat transfer coefficient and larger pressure drop. Derby et al. [29] studied condensation in copper-microchannels at high vapor mass fluxes (50–200 kg/m<sup>2</sup> s). They arranged hydrophilic strips on hydrophobic surface for bottom channel. The heat transfer coefficients in the channel with biphilic strips are even lower than those with uniform hydrophobic surface.

This paper provides a robust surface and achieves better understanding of DWC in confined channel with biphilic surface. The polymer film keeps better heat transfer performance for long-term operation. Three steps are involved to fabricate the biphilic surface. Our experiment shows that heat transfer is enhanced on biphilic surface compared to hydrophobic surface. The *directional-droplets-coalescence* is found for the first time. Besides, droplets are observed to depart faster on biphilic surface than on hydrophobic surface. These factors explain the heat transfer enhancement for DWC in mini-channels.

## 2. Materials and methods

This section contains Section 2.1 for condenser package, Section 2.2 for fabrication of condenser surface, Section 2.3 for experimental setup, and Section 2.4 for experiment procedures.

### 2.1. The condenser package

Fig. 1 shows the condenser package including four pieces: a top 7740 glass cover 1, a Teflon insulation block 5, a copper block 8 and a stainless-steel substrate 12. Pieces 1 and 5 were bonded by a sealing ring 2. Piece 8 was tightly embedded in piece 5 to form a mini-channel cross section for condensation flow. Pieces 8 and 12 were bonded by a sealing ring 11. All the components were integrated by screw tightening.

An entrance hole 3 and an exit hole 10 were arranged in the Teflon block to penetrate inlet and outlet capillary tubes for fluid transfer. There were eight thermocouple holes ( $\sim$ 1 mm diameter) to penetrate jacket thermocouples, two for fluid temperature measurements 4 and 6, and others for copper block temperature measurements. During operation, cooling water was flowing in a mini-channel of the bottom plate to dissipate heat from condenser. Fig. 1b shows the copper block with a planar size of 30.0 mm by 3.13 mm, identical to the condensation surface. In the copper block, three independent regions were separated by 0.8 mm slot gap 9. The three regions had identical surface area of  $A_1$ ,  $A_2$  and  $A_3$ . Each region had a heat flux  $q$  determined by two thermocouples. For example, for the first region,  $q_1$  is written as  $q_1 = k(T_{11} - T_{21})/l_h$ , where  $k$  is the copper thermal conductivity and  $l_h$  is the distance between the two thermocouples ( $l_h = 9.0$  mm here). Similarly,  $q_2$  and  $q_3$  were processed for second and third regions. Each jacket thermocouple was tightly inserted in the corresponding hole by filling high thermal conductivity glue. We note that thermocouples  $T_{11}$ ,  $T_{12}$  and  $T_{13}$  were located in the center location of each region along flow direction. An additional test was performed to verify the effectiveness of the surface temperature measurement by using the linear-line extension. Heat flux was applied via the bottom surface of the copper block (see Fig. 1b). Except  $T_{11}$  and  $T_{21}$ , an additional thermocouple was welded on the center of the  $A_1$  region to directly measure the surface temperature. The difference between the measured surface temperature and the linear-line extended temperature via  $T_{21}$  and  $T_{11}$  was neglectable. For example, the measured surface temperature was 258.9 °C, while the linear-line extended temperature was 258.5 °C when  $T_{21} = 269.2$  °C and  $T_{11} = 262.2$  °C. The small error induced by only two thermocouples measurement is due to the negligible variation of copper thermal conductivity in a narrow temperature range. For our formal experiment, the difference between  $T_{21}$  and  $T_{11}$  was in the range of 11–21 °C.

In this study, three condensers were tested. The data reduction is sensitive to the cross-section area of condenser channel. A smart method was developed to ensure identical cross-section areas (see Fig. 2). The channel depth  $\delta$  is paid attention, in which the target value is  $\delta = 1$  mm. The copper block was precisely fabricated,

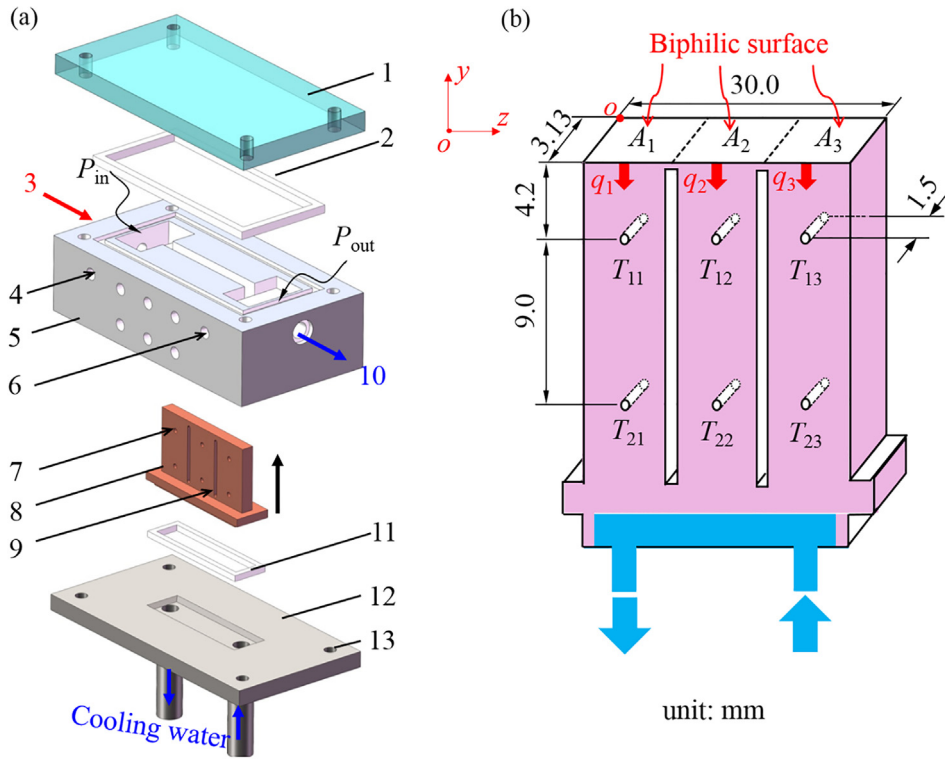


**Fig. 1.** The test section assembly (1: 7740 glass cover, 2: sealing ring, 3: inlet vapor, 4: hole for thermocouple penetration ( $T_{in}$ ), 5: Teflon for thermal insulation, 6: hole for thermocouple penetration ( $T_{out}$ ), 7: hole for thermocouple penetration ( $T_{ij}$ ), 8: copper block, 9: slot for thermal insulation, 10: outlet fluid, 11: sealing ring, 12: stainless steel substrate, 13: hole for screw tightening).

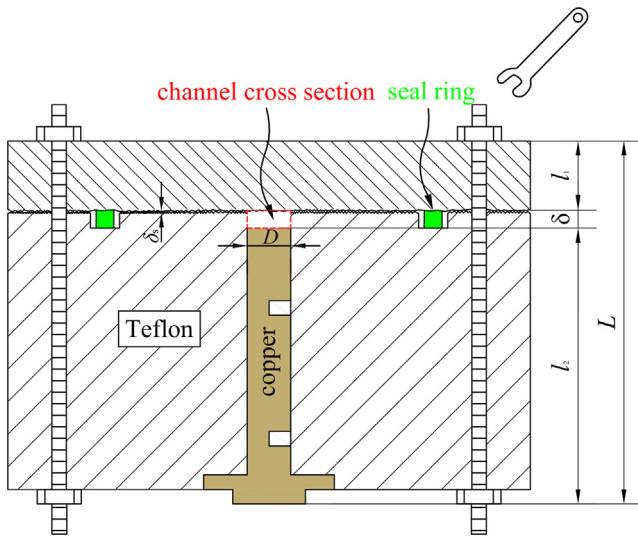


**Fig. 2.** The method to control the accuracy of mini-channel depth.

whose height was recorded as  $l_2$  to have a 0.02 mm measurement uncertainty. The glass cover thickness  $l_1$  had an uncertainty of 0.02 mm. The channel height is expressed as  $\delta = L - l_1 - l_2$ , where  $L$  is the total height from top surface of the glass cover to bottom surface of the copper block. The target channel depth is approached by adjusting  $L$  (see Table 1 for the measurement outcomes). The hydraulic diameter of the mini-channel is 1.48 mm. The maximum relative error of the cross-section areas for the three condensers is 3.34%.

**Table 1**  
Dimensions of the three mini-channels.

Dimension	Condenser		
	Mini-channel with biphilic surface	Mini-channel with hydrophobic surface	Mini-channel with hydrophilic surface
Height (mm)	$0.97^{+0.01}_{-0.01}$	$0.97^{+0.01}_{-0.01}$	$0.97^{+0.01}_{-0.01}$
Width (mm)	$3.13^{+0.01}_{-0.02}$	$3.14^{+0.01}_{-0.01}$	$3.14^{+0.01}_{-0.01}$
Cross section area (mm <sup>2</sup> )	$3.04^{+0.05}_{-0.05}$	$3.05^{+0.04}_{-0.05}$	$3.05^{+0.04}_{-0.04}$

Note: Maximum relative error of the cross-section areas for the three condensers is 3.34%.

## 2.2. Fabrication of condenser surface

The three condensers had different condenser surfaces: biphilic surface, hydrophobic surface, and hydrophilic surface polished by sand paper. The latter two surfaces were easily fabricated. Fig. 3a shows the three steps to fabricate the biphilic surface: (1) welding junction array formation by diffusion welding technique in an oven, (2) dipping the sample in Teflon solution and then baking it to coat polymer film on copper surface, and (3) separating mesh screen from copper substrate to expose hydrophilic dot array.

Fig. 3b describes the fabrication principle. Mesh screen includes straight weft wires and curved warp wires. Due to periodic structure, “point contact array” is formed if a mesh screen is put on a copper plate. When a force  $F$  is applied on the mesh screen uniformly, due to the weak deformation of warp wires, point contact array is extended to dot contact array. Sintering the bonded package in an oven at high temperature melts the “dot contact array”. The oven temperature is controlled in a range between softening temperature  $T_s$  and melting temperature  $T_m$ , at which dot EF is

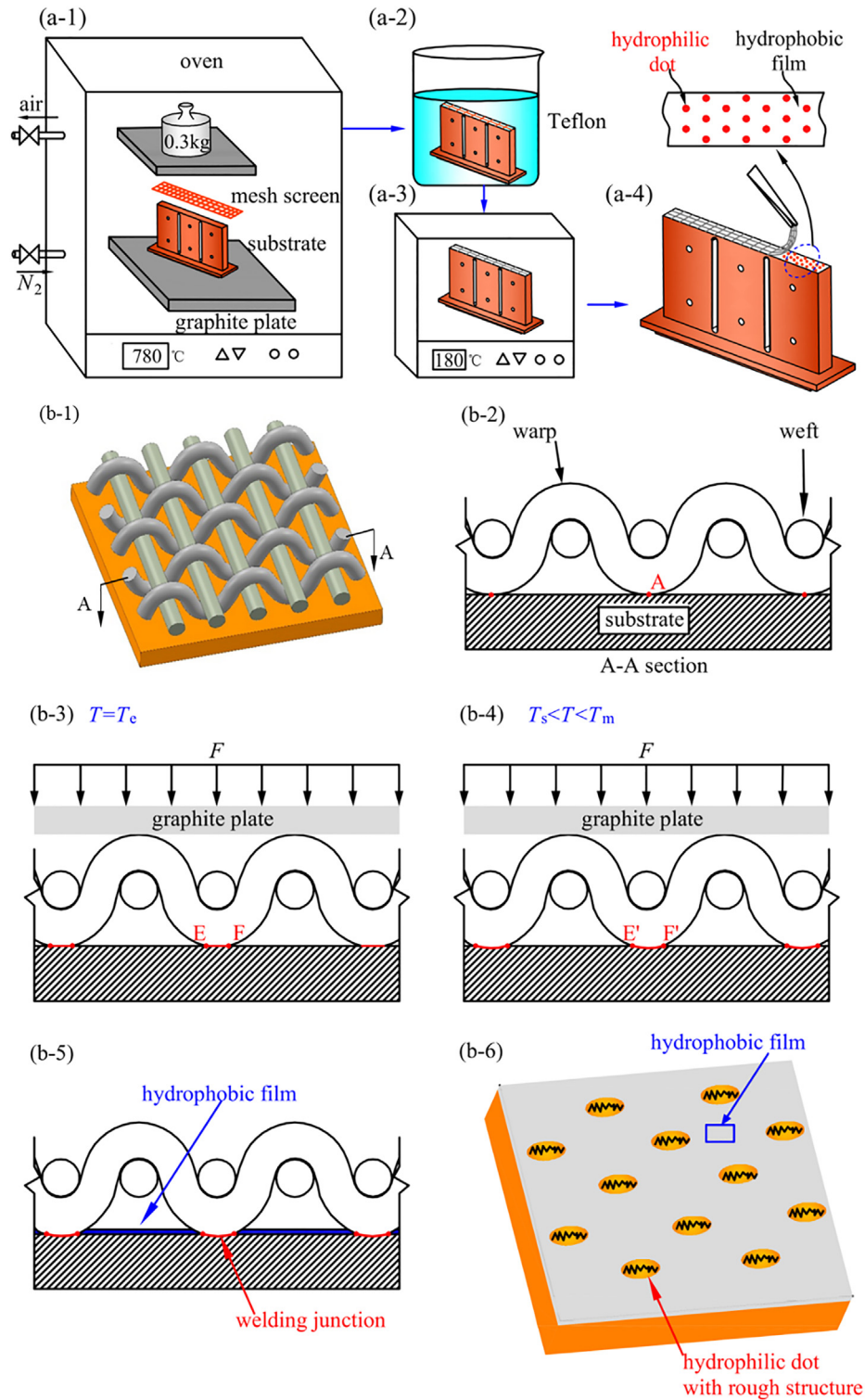


**Fig. 3.** Fabrication of biphilic surface (a-1: sintering mesh screen on copper substrate by diffusion welding technique; a-2: fabrication of hydrophobic film by dipping copper block in Teflon solution; a-3: baking copper block in an oven; a-4: exposure of hydrophilic dots by separation of mesh screen from copper substrate; b-1: mesh screen on copper substrate; b-2: point contact array forms between mesh screen and copper; b-3: dot contact array forms by applying an external force; b-4: welding junction array forms by diffusion welding; b-5: chemical treatment forms hydrophobic structure; b-6: biphilic surface is formed after tearing mesh screen from copper surface).

extended to dot E'F'. The melting areas are solidified to form welding junction array after taking out the sample. The chemical treatment of the sintered package generates polymer layer on copper surface except welding junction array. The welding junction prevents such area from exposing in Teflon solution. Tearing mesh

screen from copper surface exposes micro-dot array, which is hydrophilic.

The SEM (Scanning Electron Microscope) image is shown for mesh screen in Fig. 4a and for biphilic surface in Fig. 4b-e. The mesh screen is characterized by a mesh wire diameter  $d = 41 \mu\text{m}$

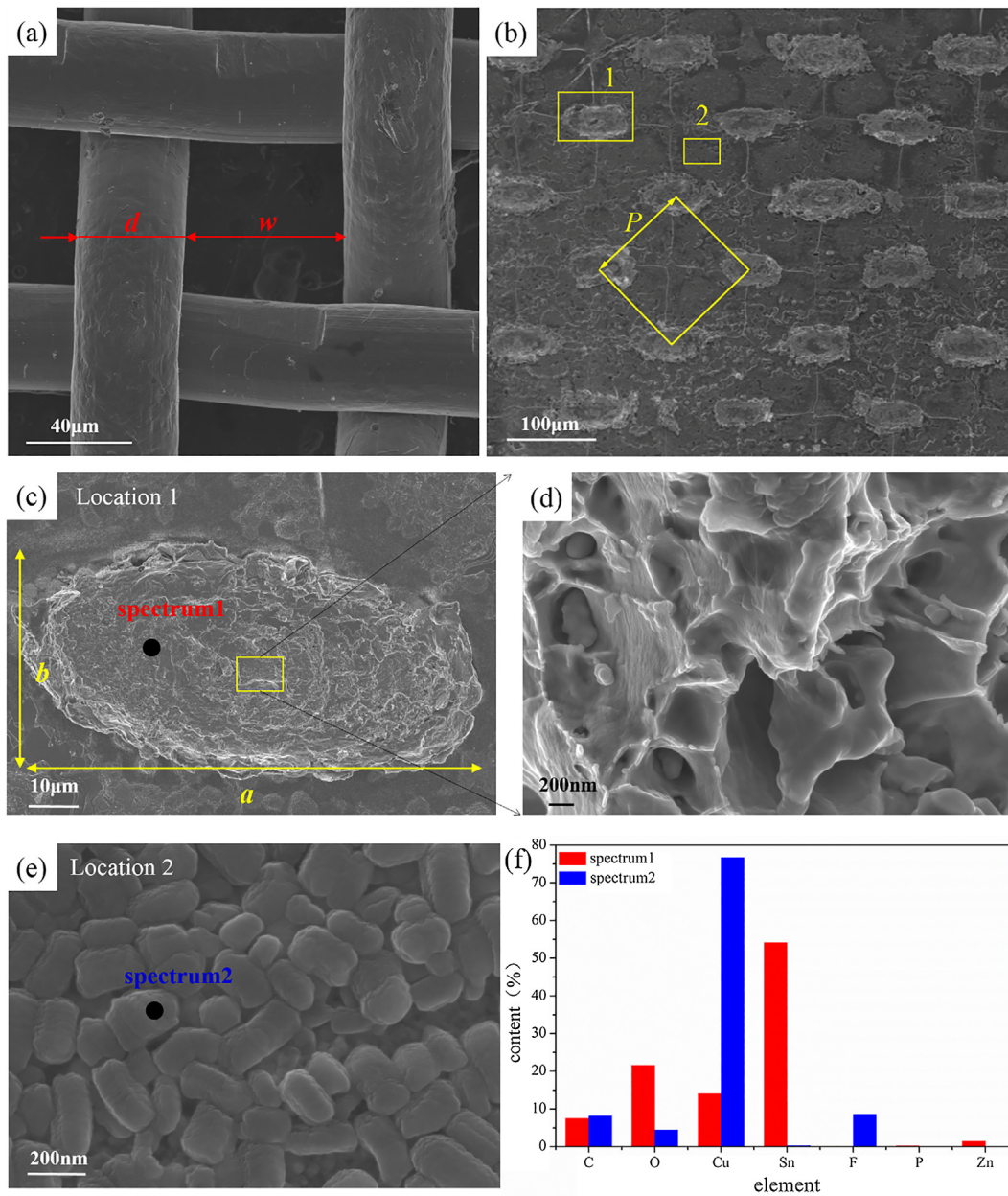


**Fig. 4.** Biphilic surface structure and element content analysis (a: characteristic sizes of the mesh screen mask, b: SEM for biphilic surface with  $P = 141 \mu\text{m}$ , c: elliptical hydrophilicity dot with  $a = 77 \mu\text{m}$  and  $b = 44 \mu\text{m}$ , d: hydrophilic dot nanostructure, e: Teflon film nanostructure, f: element spectrum of hydrophilic dot and hydrophobic film).

and a pore width  $w = 59 \mu\text{m}$ . Fig. 4b shows the micro-dot array, similar to footprints. The distance between neighboring dots is  $P = 141 \mu\text{m}$ . Each dot behaves elliptical shape, having a major axis of  $a = 77 \mu\text{m}$  and a minor axis of  $b = 44 \mu\text{m}$  (see Fig. 4c). By counting 20 micro-dots, the major axis is in the range of 63.0–91.1  $\mu\text{m}$  and the minor axis is in the range of 32.2–46.9  $\mu\text{m}$ . Correspondingly, the dot area is in the range of 2028.6–4042.8  $\mu\text{m}^2$ . The hydrophilic dot is examined to have cavity structure in a size range of 200–500 nm (see Fig. 4d). Fig. 4e shows Teflon particles deposited on copper surface. The  $\sim 100 \text{ nm}$  Teflon particles are hydrophobic to water, which are different from nano-pillars structure reported in the literature [9,10]. Fig. 4f shows element content to indicate the existence of fluorine (F) element in hydrophobic region (location 2), but the hydrophilic dot (location 1) does not have F element.

Because the conduction thermal resistance of polymer layer is related to the layer thickness, the coating layer thickness was measured by a Bruker Dektak XT stylus profile, using a surface having a polymer layer part and a bare surface part (see Fig. 5). A scratch tunnel was created across both the polymer layer part and the bare surface part. The detector 1 measured the depth  $\delta_{c1}$  from polymer surface to scratch bottom. Alternatively, the detector 2 measured the depth  $\delta_{c2}$  from bare surface to scratch bottom. Thus, the polymer layer thickness is recorded as  $\delta_c = \delta_{c1} - \delta_{c2} = 12,444 \text{ \AA}$ .

Fig. 6 shows the measured contact angles (CA) on surfaces with different wettabilities. The CA is  $74^\circ$  on polished copper surface, but decreases to  $22.6^\circ$  on hydrophilic dot. The polymer layer has CA of  $135^\circ$ . Contact angle and surface adhesion are two different concepts. Contact angle larger than  $90^\circ$  is regarded as hydrophobicity. Surface adhesion depends on droplet morphology in micro/-

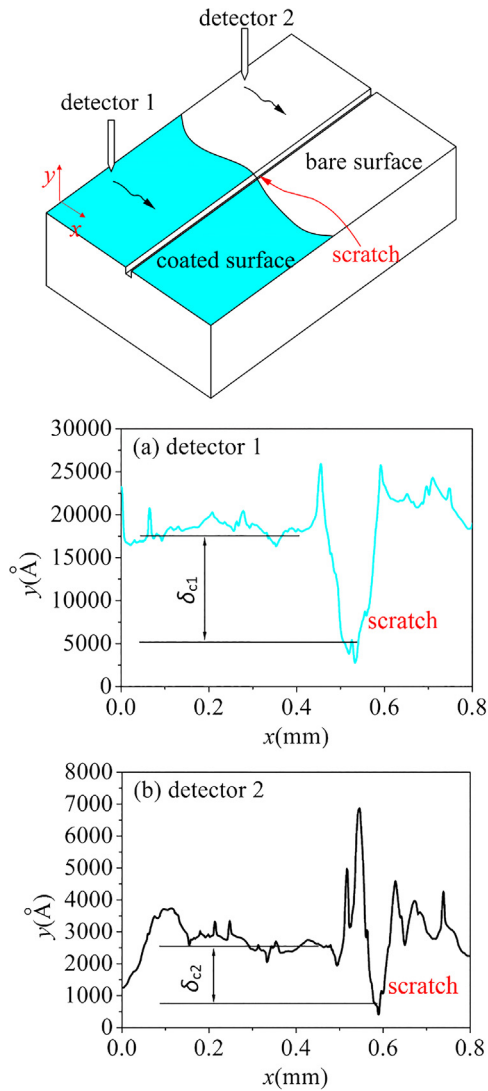


**Fig. 5.** Surface morphology measured by Bruker Dektak XT stylus profiler (a:  $\delta_{c1} = 37,918 \text{ \AA}$  of Teflon film relative to scratch depth, b:  $\delta_{c2} = 25,474 \text{ \AA}$  of copper surface relative to scratch depth, Teflon film thickness is deduced as  $\delta_c = \delta_{c1} - \delta_{c2} = 12,444 \text{ \AA}$ ).

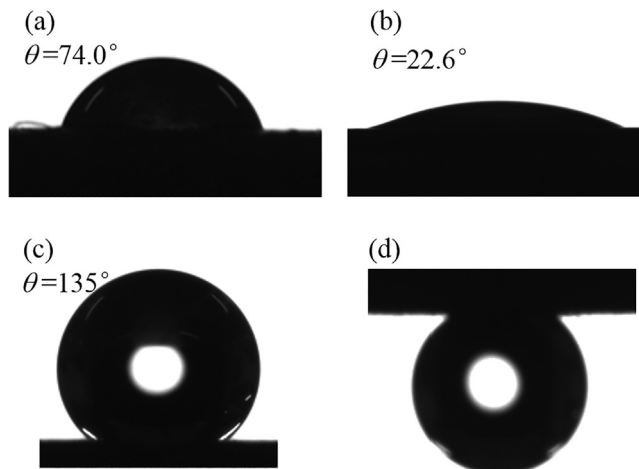


**Fig. 6.** Contact angles (CA) on various surfaces (a: CA on polished copper surface, b: CA on hydrophilic surface fabricated by diffusion welding technique, c: CA on Teflon film surface, d: high adhesion behavior of droplet on Teflon film).

nano structure of the surface. Cassie state refers to the dry micro/nano structure, but Wenzel state refers to droplet vapor-liquid interface penetrating into the micro/nano structure, thus the micro/nano structure is wet. Wenzel state corresponds to high adhesion. Here, the polymer layer film is hydrophobic but behaves high adhesion. In summary, a novel method is developed to fabricate biphilic surface. By using diffusion welding technique, the arrays of mesh screen tips are printed on copper surface. Because mesh screen is cost-effective and commercialized, the method is scalable for large scale application. Teflon (PTFE) acts as the hydrophobic part, having melting and boiling temperatures of  $327^\circ\text{C}$  and  $400^\circ\text{C}$ , respectively [30]. The decomposition temperature is up to  $415^\circ\text{C}$ , which is attractive for heat exchangers' application.

### 2.3. Experimental setup

The experiment system includes a forced convection loop, a condenser package, a cooling water loop and a data acquisition system (see Fig. 7). An electric steam boiler, a  $3 \mu\text{m}$  filter, one of the three condensers, a post-condenser are connected by stainless-steel capillary tubes. The post-condenser completely cooled two-phase mixture into water. An electric balance measured the condensed water flow rate with a resolution of  $0.02 \text{ g}$ . A pressure transducer measured the condenser inlet pressure. A differential pressure transducer measured the pressure drop across condenser inlet and outlet. The capillary tubes upstream of the condenser are wrapped by thermal insulation material. In order to compensate the heat leakage, the upstream capillary tube is wrapped by an electric wire for heat compensation, which will be discussed later. A gear pump circulated the cooling water flow rate through the condenser. Mass flow rate of cooling water and water temperatures entering and leaving the condenser were measured.

All the data were collected by a high-speed data acquisition system (DL 750, Yokogawa, Inc., Japan) with 16 channels. The data sampling rate can reach 10 million samples per second. Here, the recording rate was 100 samples per second, which is fast enough. A high-speed camera (VW-600C, KEYENCE) incorporates a stereo microscope (VW-L1) recorded the dynamic flow images.

### 2.4. Experiment procedures

**Remove of non-condensable gas:** Non-condensable gas should be removed from liquid [31]. The whole loop was vacuumed and degassed, then deionized water was charged into the steam boiler. Before condensation experiment, heating the water increased pressures in the steam boiler. A high precision pressure transducer and a safety valve were installed at the top of the steam boiler. The safety valve was set at a desired pressure such as  $\sim 3 \text{ bar}$ . When the pressure reached the desired value, the safety valve automatically discharged vapor to environment. The discharging process was stopped until the vapor pressure precisely agreed with the saturation temperature.

**Heat compensation technique:** A compensation heat was added via metallic wire to ensure pure vapor at condenser inlet (see Fig. 7). The heat leakage is influenced by thermal conduction resistances of capillary tube and thermal insulation material. The in-tube-condensation flow and the single-phase water flow behave similar heat leakage, as long as the fluid-temperatures are similar. The vapor temperature covered a range of  $101.3\text{--}114.2^\circ\text{C}$ . For single-phase water flow, the  $\sim 100^\circ\text{C}$  water temperature level was ensured. Without heat compensation,  $\Delta T_i$  is the temperature drop from steam boiler to condenser inlet, thus the dissipation heat is  $Q_{dis} = mC_{p,l}\Delta T_i$ , where  $m$  is the water flow rate and  $C_{p,l}$  is the water specific heat.  $Q_{dis}$  was about  $13.2 \text{ W}$ . During condensa-

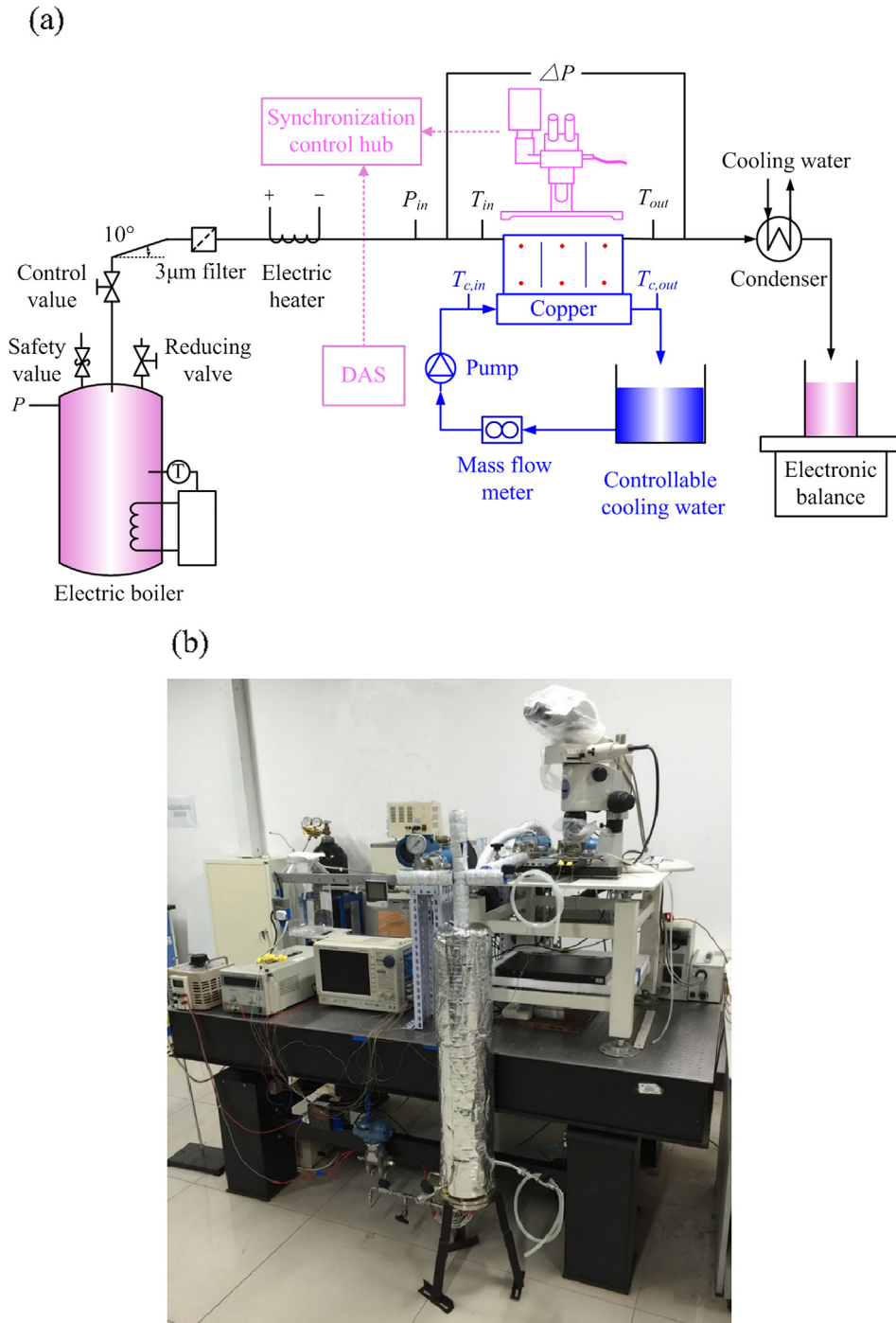


Fig. 7. Experimental setup.

tion experiment, the same heat of  $Q_{dis}$  was supplied to the upstream tube line. The effectiveness of this method was checked by the relationship between vapor pressure and temperature at condenser inlet. For a measured pressure  $P_{in} = 116.33$  kPa, the saturation temperature is  $T_{sat} = 103.59$  °C, while the measured value is 103.5 °C. No droplets were observed at condenser inlet with heat compensation.

**Data reduction and uncertainty:** Mass flux of the condensation flow is defined as  $G = m/A_c$ , where  $A_c$  is the cross-section area for each condenser (see Table 1). Three heat fluxes  $q_1$ ,  $q_2$ , and  $q_3$  are determined for three independent regions. Condensation heat transfer coefficient is

$$h_i = \frac{q_i}{T_{w,i} - T_{sat,i}} \quad (1)$$

where the subscript  $i = 1, 2, 3$ , corresponding to the centers of  $A_1$ ,  $A_2$  and  $A_3$ , respectively.  $T_w$  is linearly extended from copper block temperatures to wall location. The saturation pressure  $P_{sat,i}$  is assumed to have linear distribution along flow direction, yielding the corresponding saturation temperatures  $T_{sat,i}$  at the centers of  $A_1$ ,  $A_2$  and  $A_3$ . Eq. (1) determines the copper surface temperature. Introducing a 1.2 µm polymer layer generates a couple of degrees of temperature drop across the film, covering our present data range. Because bare copper regions and polymer layer regions are alternatively

populated on biphilic surface, it is difficult to choose the surface temperature. Thus, for all the three condensers, the copper surface temperature given in Eq. (1) is used as the reference value for comparison analysis.

The error transmission theory is applied to evaluate uncertainties of  $q$  and  $h$ . If  $Y$  is a function of independent variables  $x_1, x_2, x_3 \dots x_n$  and  $\delta x_1, \delta x_2, \delta x_3 \dots \delta x_n$  are uncertainties of independent parameters, the uncertainty of  $Y$  is

$$\delta Y = \sqrt{\left(\frac{\partial Y}{\partial x_1} \delta x_1\right)^2 + \left(\frac{\partial Y}{\partial x_2} \delta x_2\right)^2 + \dots + \left(\frac{\partial Y}{\partial x_n} \delta x_n\right)^2} \quad (2)$$

Because  $q = k\Delta T/l_h$ , the uncertainties of  $q$  is

$$\delta q = \sqrt{\left(\frac{k\delta(\Delta T)}{l_h}\right)^2 + \left(\frac{k\Delta T\delta l_h}{l_h^2}\right)^2} \quad (3)$$

where  $\delta(\Delta T)$  is the uncertainty of temperature difference between two thermocouples, each having an uncertainty of 0.2 °C. The maximum  $\delta(\Delta T)$  reaches when the higher temperature reaches positive uncertainty and the lower temperature reaches negative uncertainty, thus  $\delta(\Delta T) = 0.4$  °C. Eq. (3) gave  $\delta q = 28$  kW/m<sup>2</sup>K to have the relative uncertainty of heat flux of 4.32%. Performing the uncertainty analysis for Eq. (1) gave the relative uncertainty of heat transfer coefficient of 14.9%.

Table 2 shows the ranges and uncertainties of various parameters. Because the cases with low mass fluxes  $G$  are more interest to industry applications, the  $G$  range is 10.47–63.83 kg/m<sup>2</sup> s. In our experiment, the condenser outlet pressure approaches atmospheric pressure. Thus, the inlet pressure of the condenser  $P_{in}$  is the value that is sufficient to drive the corresponding mass flux  $G$  flowing through the condenser. Correspondingly, the inlet pressure  $P_{in}$  covers the range of  $1.05 \times 10^5$ – $1.30 \times 10^5$  Pa.

### 3. Results and discussion

The calibration experiment was performed with single-phase water flow in the mini-channel, in which the water has a temperature drop from  $T_{in}$  to  $T_{out}$ . Thermal efficiency is defined as the cooling water received heat divided by the hot water dissipated heat. The thermal efficiency is shown to be in the range of 0.92–0.98, indicating the reliability of the experiment setup. Besides, the measured filmwise condensation heat transfer coefficients in the mini-channel with polished surface are compared with the prediction given in the literature [32]. The deviation between them is found to be 18.7%, which is reasonable for two-phase flow experiment (see Supplementary Information for calibration details). This section describes the performances of the three condensers with biphilic, hydrophobic and hydrophilic surfaces, followed by the mechanism analysis.

#### 3.1. Thermal-hydraulic performances of the three condensers

Figs. 8 and 9 show condensation heat transfer coefficients  $h$  and heat fluxes  $q$  along axial flow direction  $z$ . The subscript e, o and i represent condensers using biphilic surface, hydrophobic surface and hydrophilic surface, respectively. Because  $h$  and  $q$  are influenced by vapor inlet pressure  $P_{in}$  and cooling water flow rate  $m_c$ , each subfigure shares similar  $P_{in}$  and  $m_c$ . Alternatively, Fig. 10 presents  $h_e/h_o$  and  $q_e/q_o$ : the condenser performance with biphilic surface related to hydrophobic surface. Each subfigure of Figs. 8 and 9 refers to a specific run, during which the inlet pressure  $P_{in}$  and cooling water flow rate  $m_c$  are slightly oscillating. Thus, the range including the minimum and maximum values is given. In fact, the oscillating range is very narrow. The difference between maximum and minimum values are smaller than 4.6% covering the whole data range.

##### 3.1.1. Best performance with biphilic surface

Figs. 8–10 show that the biphilic surface has largest heat transfer coefficient  $h_e$  and heat flux  $q_e$  among the three condenser surfaces. The performance curve of hydrophobic surface is between the top margin specified by biphilic surface and bottom margin given by hydrophilic surface (see Figs. 8 and 9). For hydrophilic surface, heat transfer coefficients decrease along flow direction, due to increased liquid film thicknesses, matching the classical FWC analysis. The other two surfaces hold DWC, for which droplets are two-dimensional cake shape in mini-channels. Decreased heat transfer coefficients along flow direction are caused by increased footprint area of droplets on the surface.

The heat flux distribution is different from that of heat transfer coefficient. The biphilic surface has largest heat fluxes among the three condensers. On biphilic surface,  $q$  is increased from first to second region, and weakly changes from second to third region, indicating better performance along the whole flow length. However, such distribution is changed on hydrophobic and hydrophilic surfaces. On hydrophobic surface, heat fluxes display parabola shape:  $q$  is largest in the middle region, but are smaller in first and third regions. On hydrophilic surface,  $q$  can either be decreased or increased (see Fig. 9). Heat flux is the outcome of condensation heat transfer coefficient and temperature difference between two-phase mixture and wall. Smaller  $P_{in}$  in condenser corresponds to smaller vapor mass flux to yield decreased heat flux distribution (see Fig. 9a and c). For larger  $P_{in}$ , the increased vapor mass flux decreases water film thickness to strengthen heat transfer, yielding increased heat flux distribution along flow length (see Fig. 9b, d and e).

Fig. 10 shows that the ratio of condensation heat transfer coefficient on biphilic surface relative to hydrophobic surface,  $h_e/h_o$ , is larger than 1, which is also true for the ratio of heat fluxes. The maximum  $h_e/h_o$  attains 1.89 to indicate 89% improvement of heat transfer coefficient on biphilic surface. The maximum  $q_e/q_o$  attains

**Table 2**  
Parameters, instruments and uncertainties.

Parameters	Instrument measurement or calculated	Ranges	Uncertainties
$A_c$ : cross-section area	Decided by channel width and depth	/	3.34%
$G$ : mass flux	Measured by electronic balance over time	10.47–63.83 kg/m <sup>2</sup> s	0.74–5.74%
$h$ : condensation heat transfer coefficient	Determined by Eq. (1)	$1.80 \times 10^4$ – $3.01 \times 10^5$ W/m <sup>2</sup> K	14.9%
$m_c$ : cooling water flow rate,	Coriolis mass flow meter (DMF-1-1AB)	0.89–1.49 g/s	0.6%
$P_{in}$ : pressure at condenser inlet	Pressure transducer (Rosemount-3051)	$1.05 \times 10^5$ – $1.30 \times 10^5$ Pa	0.1%
$\Delta P$ : pressure drop	Differential pressure transducer (Rosemount-3051)	$1.17 \times 10^2$ – $3.06 \times 10^3$ Pa	0.1%
$q$ : heat flux	Determined by temperature measurements	488.99–970.60 kW/m <sup>2</sup>	4.32%
$T_{in}$ and $T_{out}$ : fluid temperatures at condenser inlet and outlet	K-type thermocouple	100.0–107.2 °C	0.2 °C
$T_{11}, T_{12}, T_{13}, T_{21}, T_{22}, T_{23}$ : copper block temperatures	K-type thermocouple	52.7–99.7 °C	0.2 °C
$\delta_c$ : Teflon film thickness	Bruker Dektak	/	0.5 nm

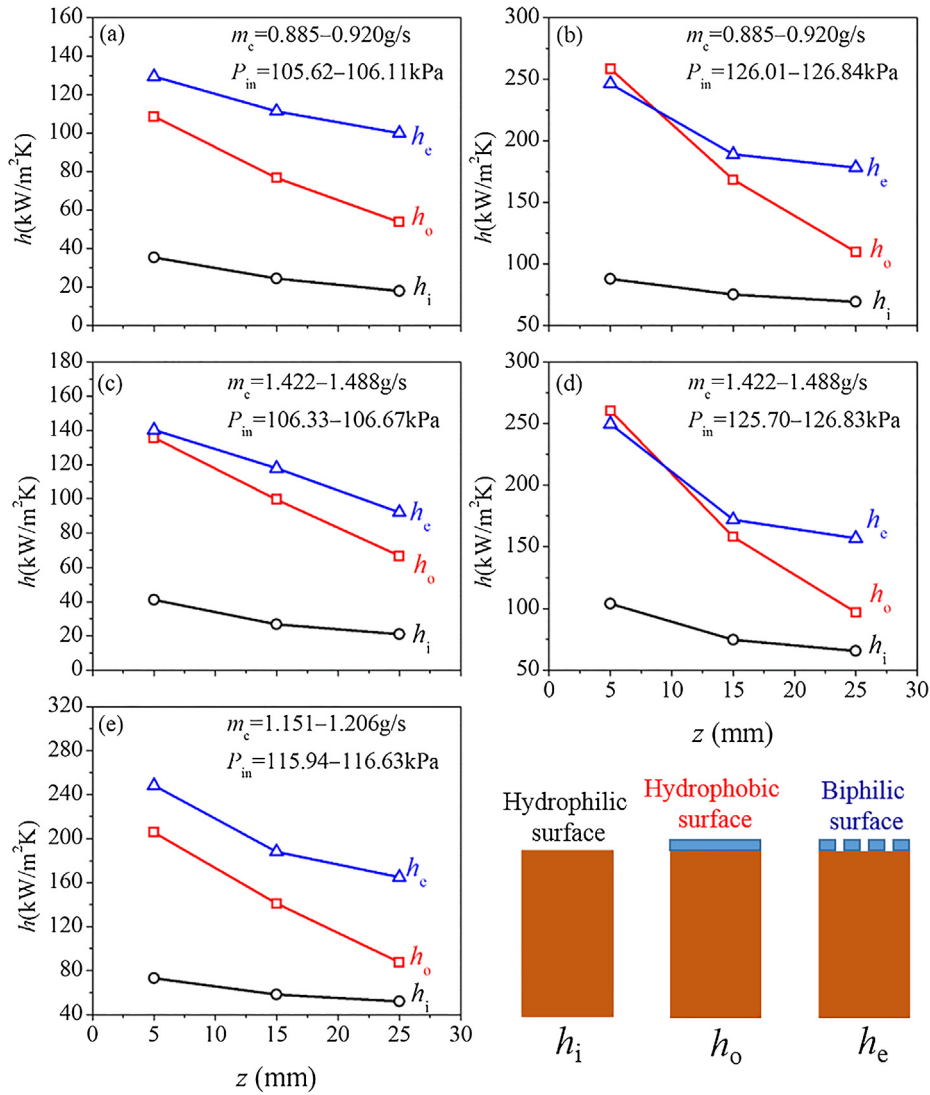


Fig. 8. Condensation heat transfer coefficients along flow direction in three mini-channels having different wettabilities.

1.40. Both  $h_e/h_o$  and  $q_e/q_o$  behave band distribution and increase trend along flow length. The values of  $h$  and  $q$  are plotted versus vapor mass qualities  $X$  in Fig. 11, showing the increase trend. The difference among the three condensers is larger at lower vapor mass qualities, indicating biphilic surface is more effective in the condenser downstream.

Attention is paid to the decayed thermal performance in the mini-channel condenser with biphilic surface. The same running cases were retested after four weeks operation (see Fig. S3 in Supplementary Information). It is shown that the experiment was repeatable and the maximum decay of heat transfer coefficients is within 20%. Considering the maximum uncertainty of heat transfer coefficient of 14.9%, the performance decay using the biphilic surface is weak.

### 3.1.2. Flow length dependent heat transfer enhancement degrees

Mini-difference of heat transfer coefficients between biphilic surface and hydrophobic surface exists in first region, but the difference becomes larger in third region. Section 3.3 describes the heat transfer enhancement mechanisms with biphilic surface: (1) easier drop nucleation due to hydrophilic dot, (2) altered droplet morphology and detachment, and (3) reduced thermal resistance due to droplet footprint on mixed surface pattern. The contribution

of the three heat transfer enhancement mechanisms depends on vapor mass flux and vapor mass qualities. In the condenser upstream, vapor mass quality is high and droplets are less. Heat transfer enhancement is majorly contributed by the increased droplet nucleation densities with biphilic surface. With the development of condensation flow, vapor mass quality is decreased and more droplets exist in the channel, the three mechanisms are combined to increase heat transfer enhancement degree.

### 3.2. Hydraulic performances of the three condensers

Pressure drop across a condenser is interest to users. Fig. 12 shows mass fluxes  $G$  versus pressure drops  $\Delta P$ , showing small difference among the three condensers. The condenser with hydrophilic surface behaves slightly better performance with slightly larger  $G$  than the other two condensers for identical  $\Delta P$ . The condensers with hydrophobic surface and biphilic surface share similar pressure drops. Pressure drop is dependent on flow patterns. For FWC on hydrophilic surface, the whole channel surface is covered by liquid film. Pressure drop is proportional to shear stress between wall and liquid. For DWC on other two surfaces, part of channel wall is covered by vapor and the remaining is covered by droplets. Pressure drop is dominated by two effects. The vapor

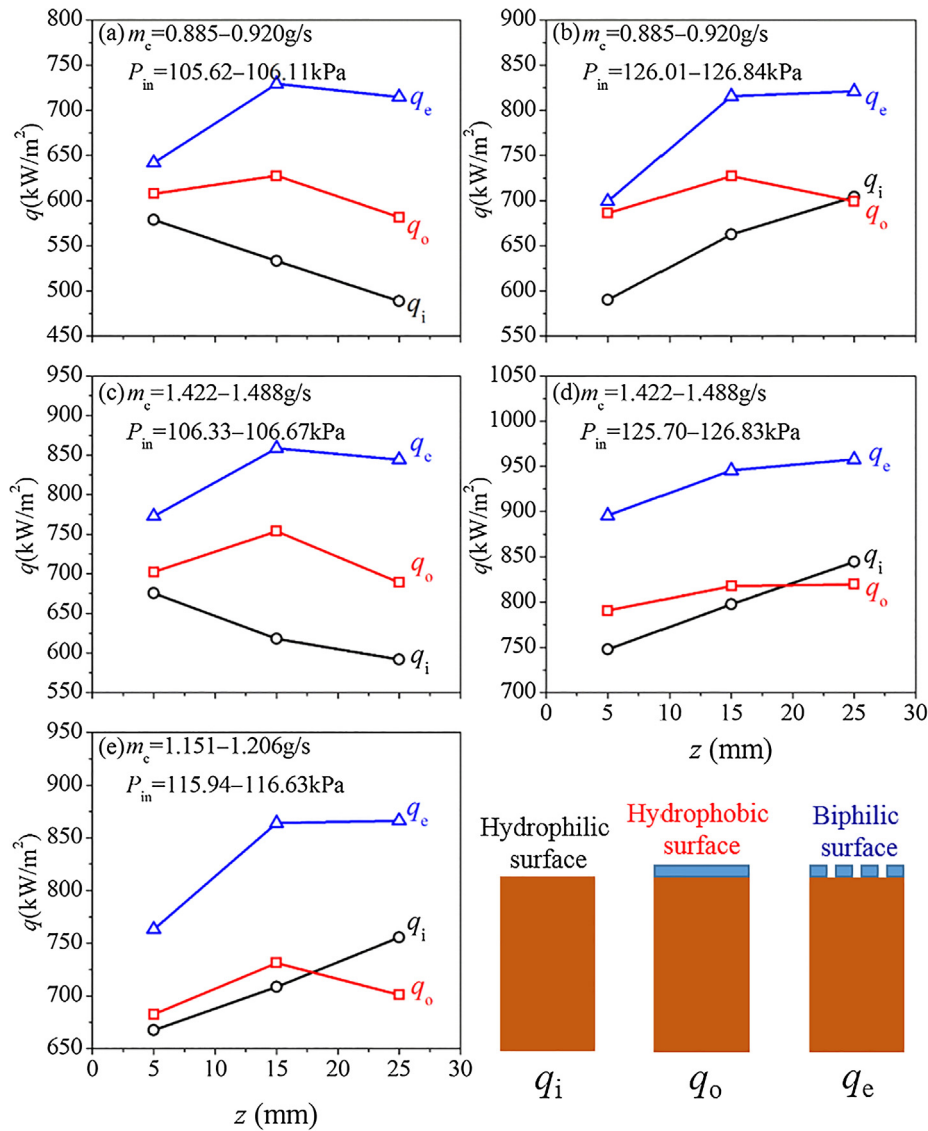


Fig. 9. Condensation heat fluxes along flow direction in three mini-channels having different wettabilities.

covered portion decreases pressure drop, but the droplets covered part increases pressure drop. The comprehensive effects cause weak difference of pressure drops among the three condensers. Two data points (one in Fig. 12a and the other in Fig. 12c) deviate from the normal curve distribution, which are caused by experiment contingency due to the complicated condensing flow in the mini-channel.

### 3.3. The mechanism analysis

#### 3.3.1. Enhanced drop nucleation and growth on biphilic surface

The minimum energy barrier for drop nucleation is written as [33]

$$\Delta G = \frac{\cos^3 \theta - 3 \cos \theta + 2}{3} \pi \sigma r_{\min}^2 \quad (4)$$

where  $\theta$  is the contact angle and  $r_{\min}$  is the minimum nucleation radius. For biphilic surface fabrication, micro-dots become rough when mesh screen is being teared from copper. Contact angle becomes  $\theta = 22.6^\circ$  on these local regions compared to  $\theta = 74.0^\circ$  on smooth copper surface (see Figs. 4 and 6).  $\Delta G$  is decreased by 98.6% when  $\theta$  decreases from  $74.0^\circ$  to  $22.6^\circ$ , explaining easier drop

nucleation on roughed hydrophilic dots compared to smooth surface. The roughness of hydrophilic dot also increases the number of drop nucleation sites  $N_c$ , which is  $f$  times of that on smooth surface, where  $f$  is the surface roughness, defined as extended fin area relative to base surface area [34].

An additional DWC experiment was performed in humid air environment, with air humidity 52.5%, environment temperature  $21^\circ\text{C}$  and wall subcooling  $13^\circ\text{C}$ . Drop nucleation was visualized by a highly magnified micro-lens camera. Fig. 13 shows the visualization area including twelve hydrophilic dots. Yellow and white envelopes represent droplets on hydrophilic dots and hydrophobic region, respectively. Droplets on hydrophilic dots are always larger than those on hydrophobic regions. Our work indicates that hydrophilic dots promote drop nucleation and growth, supporting the findings reported in Refs. [16,19].

#### 3.3.2. Directional-droplets-coalescence

When a droplet on a hydrophilic dot expands its footprint to hydrophilic dot margin, the droplet becomes the center to attract and merge neighboring droplets. For larger neighboring droplet, the droplet footprint may cover several hydrophilic dots. No matter how big a neighboring droplet is, it is moving towards the center

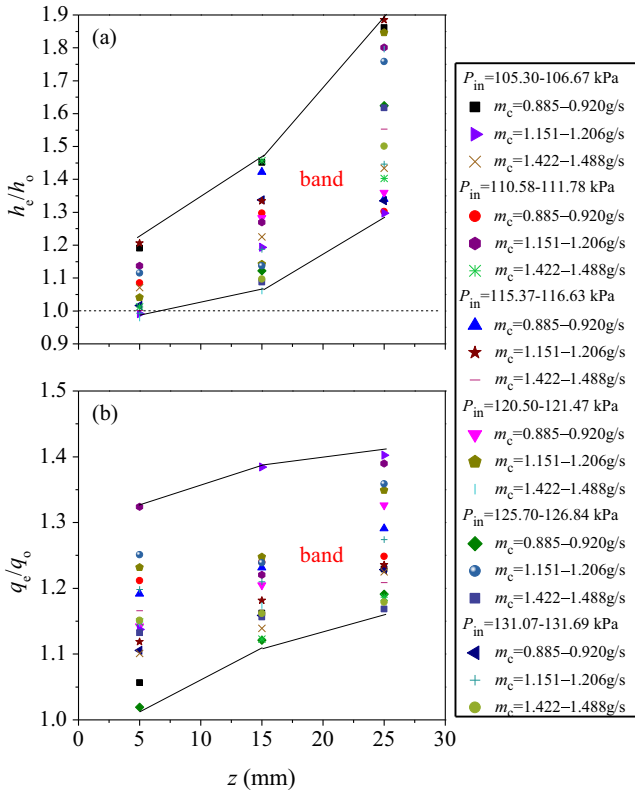


Fig. 10. Heat transfer enhancement by using biphilic surface compared with hydrophobic surface.

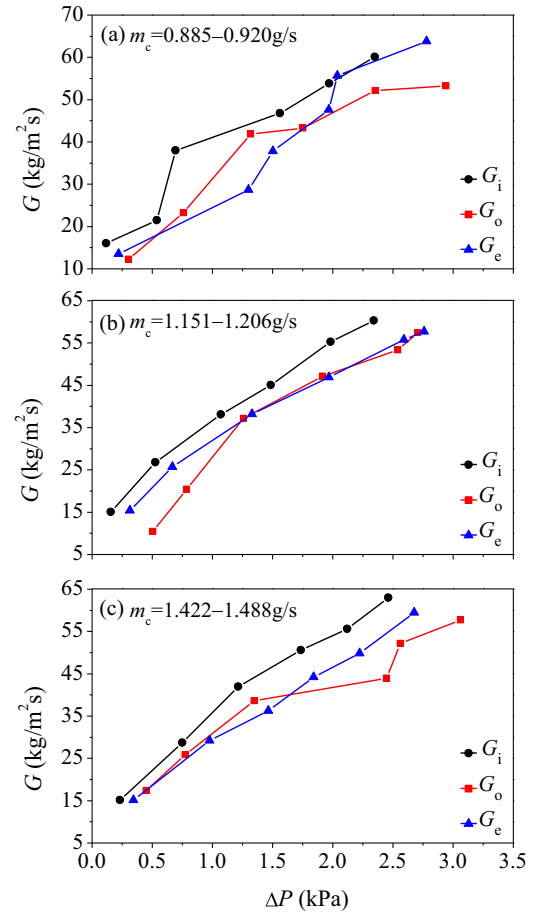


Fig. 12. Hydraulic performances of the three mini-channels having different wettabilities.

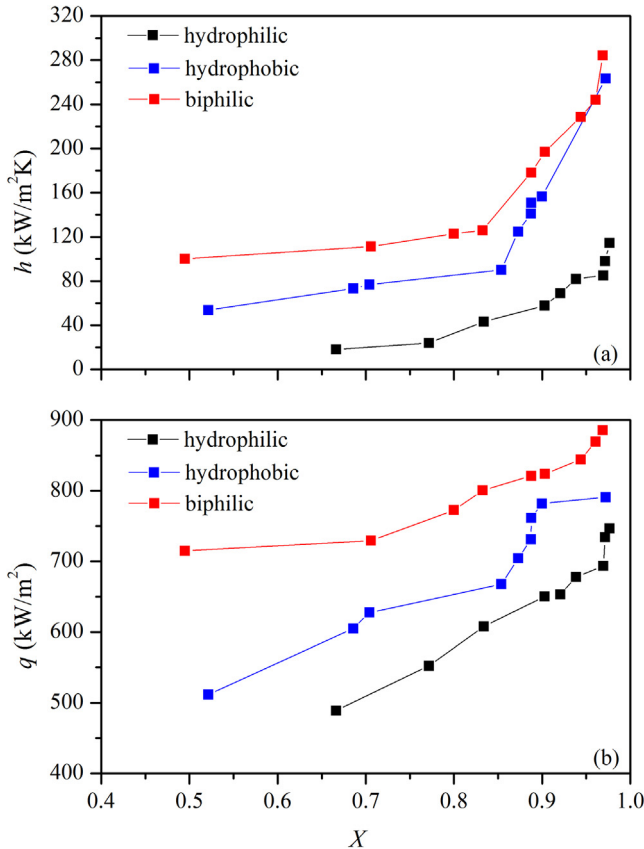


Fig. 11. Condensation heat transfer coefficients (a) and heat fluxes (b) versus vapor qualities in three mini-channels having different wettabilities.

droplet, which is called *directional-droplets-coalescence* (see Fig. 14). For a larger droplet on biphilic surface, because the contact line may cross both hydrophilic region and hydrophobic region, the droplet footprint shows irregular pattern (not smooth). Fig. 15 shows thoroughly different droplet dynamics on hydrophobic surface. Larger droplet eats smaller droplet. The droplets coalescence does not behave directional characteristic. The droplet footprint is smooth due to uniform wettability.

The *directional-droplets-coalescence* is explained by surface energy analysis (see Fig. 16). Static contact angles in hydrophilic region and hydrophobic region are recorded as  $\theta_A$  and  $\theta_B$ , respectively. Initially, droplet A is within hydrophilic dot. Droplet B is within hydrophobic region, but its contact line reaches hydrophilic margin at point P (see Fig. 16a). The surface energy analysis yields the driving force for droplet B motion [30]:

$$F_d = \sigma(\cos \theta_A - \cos \theta_B) \tag{5}$$

Thus, droplet B is moving from initial location OP to ending location TR, and droplet B becomes B' (see Fig. 16b). Because the droplet internal pressure is easily balanced [35], such motion occurs at a constant contact angle  $\theta_{B'}$  along the whole drop footprint, even though the droplet crosses both hydrophobic and hydrophilic regions [36]:

$$\theta_{B'}^2 = \frac{1}{2}(\theta_A^2 + \theta_B^2) \tag{6}$$

Substituting  $\theta_A = 22.6^\circ$  and  $\theta_B = 135^\circ$  into Eq. (6) yields  $\theta_{B'} = 96.8^\circ$ . This process stops when droplet B' contacts droplet A at point R (see Fig. 16b).

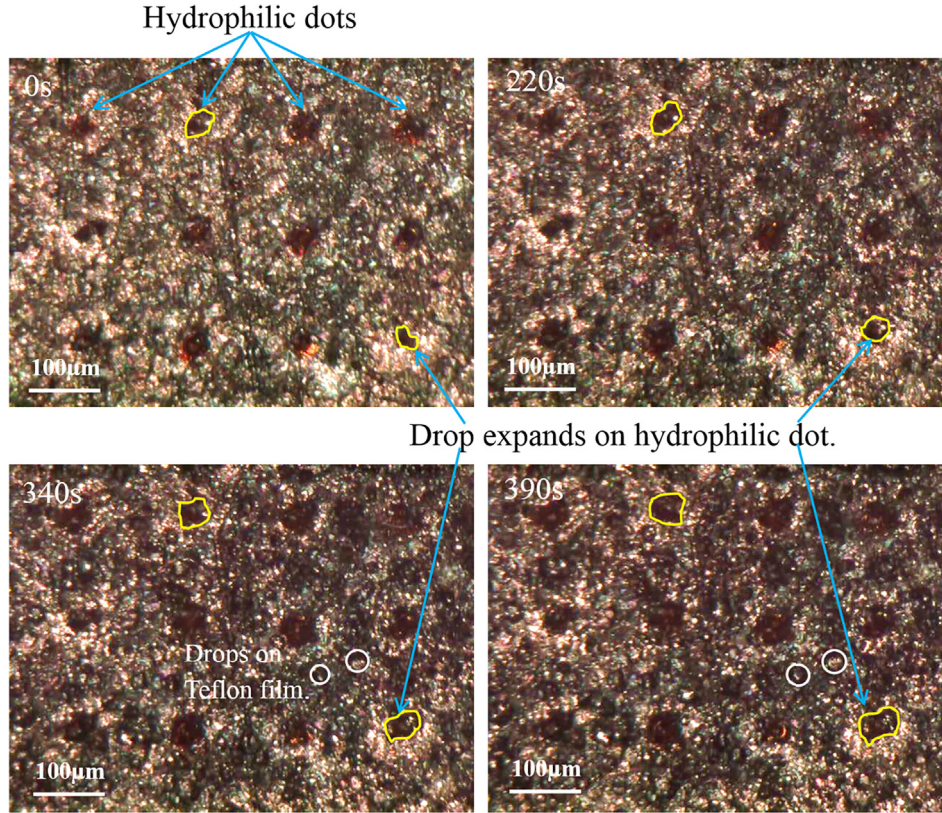


**Fig. 13.** Experiment evidence of preferential drop nucleation on hydrophilic dots (experiment was performed in 52.5% humidity wet air environment with air temperature of 21 °C and condensation surface temperature of 8 °C).

Before we deal with droplets coalescence, we examine how contact angle influences Gibbs free energy  $G_d$  [37]:

$$G_d = \sqrt[3]{9\pi V^2} \sigma f(\theta), \quad f(\theta) = \sqrt[3]{\cos^3 \theta - 3 \cos \theta + 2} \quad (7)$$

$$f'(\theta) = \frac{\sin^3 \theta}{\sqrt[3]{(\cos^3 \theta - 3 \cos \theta + 2)^2}} \quad (8)$$

where  $V$  is the droplet volume. Eq. (8) shows  $f'(\theta) > 0$  with  $\theta \in [0, \pi]$ , indicating increased  $G_d$  with increase of  $\theta$ . The droplet motion should satisfy the minimum energy principle [38]. The droplets coalescence ensures the merged droplet  $C$  moving towards hydrophilic region due to the minimum surface energy there (see Fig. 16c). The merged droplet  $C$  is stabilized at location  $SQ$ , where  $S$  is in hydrophobic region at contact angle  $\theta_{C1}$ , and  $Q$  is on hydrophilic/hydrophobic margin at contact angle  $\theta_{C2}$ . Because droplet  $C$  is pinned at point  $Q$ , the following criterion exists.

$$\theta_{re,hi} = 13.5^\circ < \theta_{C2} = \theta_B = 96.8^\circ < \theta_{ad,ho} = 148.3^\circ \quad (9)$$

where  $\theta_{re,hi}$  is the receding contact angle in hydrophilic region,  $\theta_{ad,ho}$  is the advancing contact angle in hydrophobic region. The contact angle  $\theta_{C1}$  at point  $S$  is the receding contact angle on hydrophobic surface, here  $\theta_{C1} = 111.6^\circ$ . The advancing and receding contact angles came from our measurement.

### 3.3.3. Faster droplet departure on biphilic surface

For DWC on biphilic surface, a cycle starts from drop nucleation and growth on a specific hydrophilic dot, which becomes a center to attract and merge neighboring droplets to form a large droplet, whose footprint may cover several hydrophilic dots. Once the droplet has sufficient surface area, it sharply departs due to shear stress of incoming vapor stream. Then, a new cycle begins. DWC on hydrophobic surface also shows cyclic behavior. Fig. 17 shows

that droplets depart faster on biphilic surface than on hydrophobic surface. Shortened cycle periods are observed with biphilic surface. The difference of cycle periods between the two surfaces depends on  $P_{in}$  and  $m_c$ .  $P_{in}$  determines vapor velocity to affect shear stress applied on droplet, and  $m_c$  influences vapor mass qualities. Droplet departs with sliding mode. Other modes such as jumping and rolling occurring in open environment [39,40] does not exist in mini-channel condensers.

### 3.3.4. Reduced droplet thermal resistance with biphilic surface

A growing droplet includes four thermal resistances: interface curvature thermal resistance  $R_c$ , vapor-liquid interface thermal resistance  $R_i$ , drop thermal conduction resistance  $R_d$ , and coating layer thermal conduction resistance  $R_p$  (see Fig. 18):

$$R_c = \frac{2\sigma T_{sat}}{Qr\rho_l h_{lv}} \quad (10)$$

where  $Q$  is the heat transfer rate,  $r$  is the drop radius,  $\rho_l$  is the liquid density, and  $h_{lv}$  is the latent heat of evaporation.  $R_i$  is

$$R_i = \frac{1}{2\pi r^2 h_{int}(1 - \cos \theta)} \quad (11)$$

where  $h_{int}$  is the heat transfer coefficient at vapor-liquid interface:

$$h_{int} = \frac{2\sigma_c}{2 - \sigma_c} \sqrt{\frac{M}{2\pi R T_{sat}}} \frac{\rho_v h_{lv}^2}{T_{sat}} \quad (12)$$

where  $\sigma_c$  is the condensation coefficient, which is 1 for pure vapor condensation.  $M$  is the molecular weight,  $R$  is the gas constant and  $\rho_v$  is the vapor density. Drop conduction resistance is

$$R_d = \frac{\theta}{4\pi r \lambda_i \sin \theta} \quad (13)$$

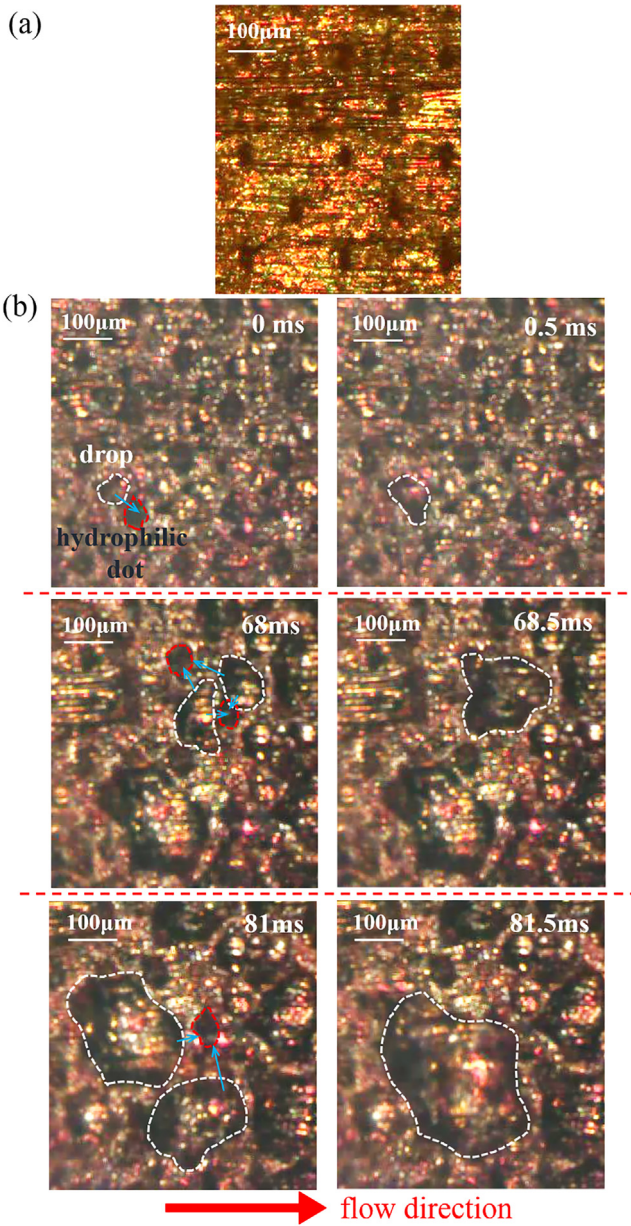


**Fig. 14.** Directional-droplets-coalescence on biphilic surface (a: dryly biphilic surface, b: droplet on hydrophilic dot eats neighboring droplet to cause directional-droplets-coalescence, red and white circles represent droplets on hydrophilic dot and biphilic surface, respectively,  $P_{in} = 105.62\text{--}106.11$  kPa,  $m_c = 0.885\text{--}0.920$  g/s, visualization area located in the middle of the whole mini-channel area).

where  $\lambda_l$  is the thermal conductivity of liquid. The additional coating layer resistance is

$$R_p = \frac{\delta_c}{\pi r^2 \sin^2 \theta \lambda_p} \quad (14)$$

where  $\lambda_p$  is the thermal conductivity of Teflon polymer.

The total droplet thermal resistance is  $R_{tot} = R_c + R_l + R_d + R_p$ . The droplet volume  $V$  and contact angle  $\theta$  has the following relationship:

$$V = \frac{\pi r^3}{3} (2 - 3 \cos \theta + \cos^3 \theta) \quad (15)$$

The comparison of  $R$  between hydrophobic surface and biphilic surface was performed. A same  $V = 0.03 \text{ mm}^3$  was assumed. On hydrophobic surface,  $\theta = 135^\circ$  yields  $r = 0.197 \text{ mm}$ . Holding  $r$  and

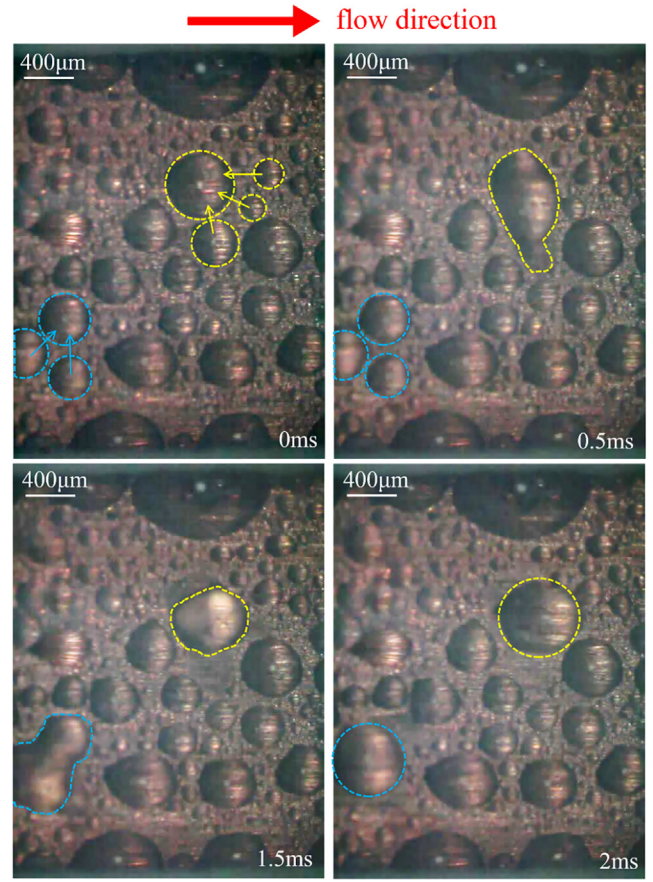
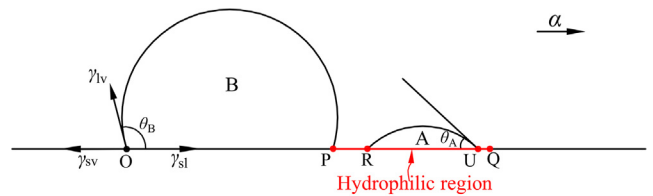
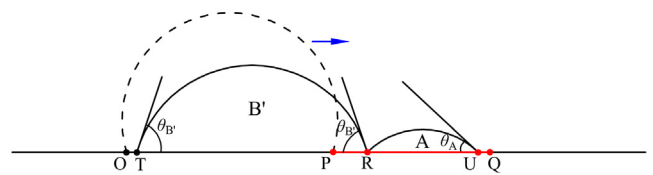


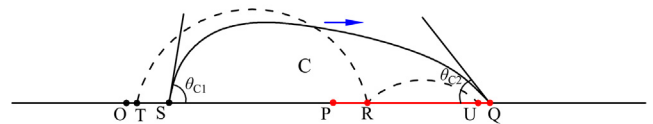
**Fig. 15.** Random-droplets-coalescence on hydrophobic surface with  $P_{in} = 105.62\text{--}106.11$  kPa and  $m_c = 0.885\text{--}0.920$  g/s.



(a) Drop B contacts hydrophilic region.



(b) Deformation and motion of drop B



(c) The coalesced drop

**Fig. 16.** High-energy-hydrophilicity-dot induced directional-droplets-coalescence.

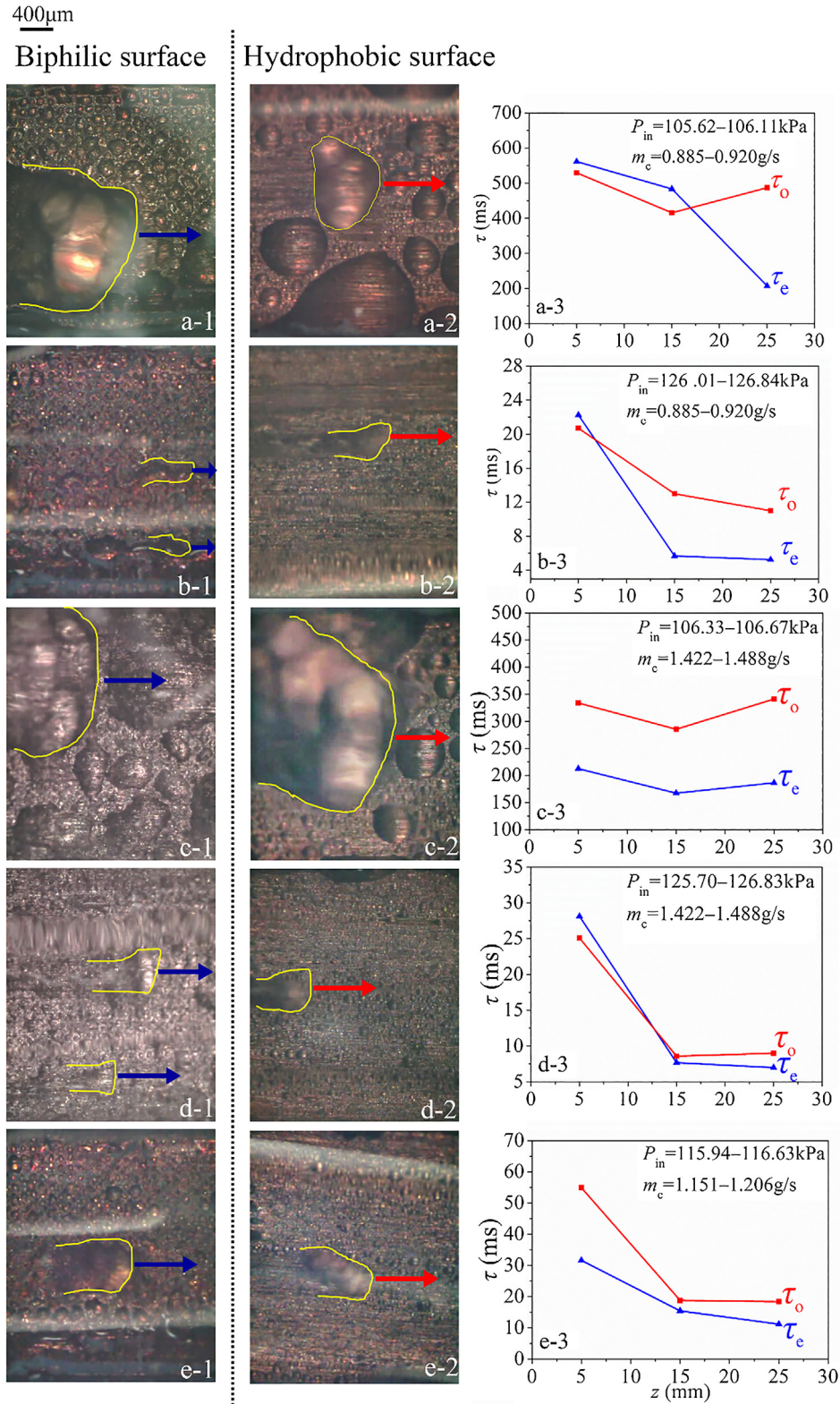


Fig. 17. Shortened droplet removal periods on biphilic surface compared with hydrophobic surface (example videos corresponding to c-1 and c-2 are provided in Supplementary Information).

$\theta$ , the four thermal resistances are  $R_c = 1.22 \times 10^{-3} \text{ K/W}$ ,  $R_i = 4.39 \times 10^{-3} \text{ K/W}$ ,  $R_d = 1.98 \times 10^3 \text{ K/W}$ ,  $R_p = 8.83 \times 10^1 \text{ K/W}$ . The total thermal resistance is  $R_{tot} = 2.07 \times 10^3 \text{ K/W}$ .

The situation becomes complicated for droplet on biphilic surface. When a droplet covers both hydrophobic region

and hydrophilic region, the droplet is un-symmetry because the two contact angles in the two regions are different. In order to simplify the thermal resistance analysis, we assume a uniform contact angle along the whole droplet footprint, which is

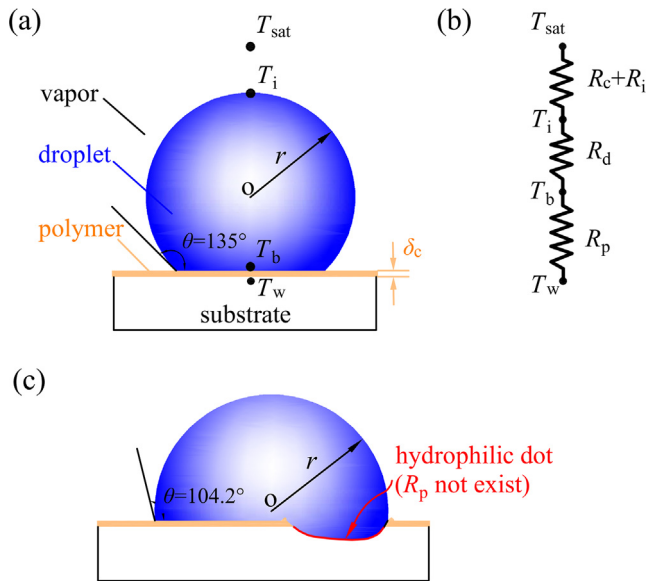


Fig. 18. Reduced thermal resistance of droplet condensation on biphilic surface compared with hydrophobic surface.

$$\theta = \frac{1}{2}(\theta_{C1} + \theta_{C2}) \quad (16)$$

Substituting  $\theta_{C1} = 111.6^\circ$  and  $\theta_{C2} = 96.8^\circ$  into Eq. (16) gives  $\theta = 104.2^\circ$ . Holding  $V$  and  $\theta$ , the biphilic surface slightly enlarges  $r$  to 0.219 mm. Thus,  $R_c$ ,  $R_i$  and  $R_d$  are computed by Eqs. (10), (11) and (13), respectively, yielding  $R_c = 8.83 \times 10^{-4}$  K/W,  $R_i = 4.84 \times 10^{-3}$  K/W and  $R_d = 1.00 \times 10^3$  K/W.

The thermal resistance calculation due to polymer layer conduction involves two steps. The first step calculates  $R_p$  using  $r$  and  $\theta$  for biphilic surface to have  $R_p = 3.78 \times 10^1$  K/W. Because  $R_p$  relates to droplet footprint area on polymer layer, the second step deduces conduction thermal resistance as the value given in the first step multiplying the ratio of hydrophobic region divided by the whole footprint area, yielding  $R_p = 3.36 \times 10^1$  K/W to have  $R_{tot} = 1.04 \times 10^3$  K/W. Compared to hydrophobic surface, biphilic surface decreases resistance  $R_p$  by 62.0%, which is due to the existence of hydrophilic dot. Biphilic surface also decreases  $R_c$  by 27.9% and  $R_d$  by 49.5%. In summary, biphilic decreases the total thermal resistance by 50.0% at  $V = 0.03 \text{ mm}^3$ , noting the reduced thermal resistance dependent on droplet size.

#### 4. Conclusion

Conclusions can be drawn as follows:

- Robust biphilic surface is fabricated. Mesh screen is sintered on copper substrate to form welding junction array. Dipping the sample in Teflon solution forms hydrophobic coating film. Separating mesh screen from copper exposes hydrophilic micro-dots array.
- Condensation heat transfer coefficients on biphilic surface are  $\sim 5.54$  times of polished copper surface, and 1.89 times of polymer layer surface, maximally. Pressure drops are almost the same for condensers using biphilic surface and hydrophobic surface.
- *Directional-droplets-coalescence* is found for DWC on biphilic surface. Droplet on hydrophilic dot becomes the center to attract and merge neighboring droplets. Droplets depart faster on biphilic surface than on hydrophobic surface.

- Droplet thermal resistance is reduced with biphilic surface. The sub-layer conduction resistance is reduced due to the existence of hydrophilic dots, which is the direct effect. Besides, the biphilic surface changes drop radius and contact angle to reduce resistances for other components, which are the indirect effect to decrease thermal resistance.
- The improved heat transfer performance using biphilic surface is due to the combined effects of altered drop dynamics including drop nucleation, growth, coalescence, departure and decreased thermal resistance of droplets.

#### Conflict of interest

The authors declared that there is no conflict of interest.

#### Acknowledgement

This work was supported by National Natural Science Foundation of China with contract numbers of 51676071 and 51436004.

#### Appendix A. Supplementary material

Supplementary data associated with this article can be found, in the online version, at <https://doi.org/10.1016/j.ijheatmasstransfer.2019.01.015>.

#### References

- [1] S. Cao, J. Xu, Y. Li, Y. Yan, Condensation heat transfer of R245fa in a shell-tube heat exchanger at slightly inclined angles, *Int. J. Therm. Sci.* 115 (2017) 197–209.
- [2] A.R. Parker, C.R. Lawrence, Water capture by a desert beetle, *Nature* 414 (2001) 33–34.
- [3] S. Choo, H.J. Choi, H. Lee, Water-collecting behavior of nanostructured surfaces with special wettability, *Appl. Surf. Sci.* 324 (2015) 563–568.
- [4] X. Ji, J. Xu, H. Li, G. Huang, Switchable heat transfer mechanisms of nucleation and convection by wettability match of evaporator and condenser for heat pipes: nano-structured surface effect, *Nano Energy* 38 (2017) 313–325.
- [5] E. Schmidt, W. Schurig, W. Sellschopp, Versuche über die Kondensation von Wasserdampf in Film- und Tropfenform, *Tech. Mech. Thermodyn.* 1 (1930) 53–63.
- [6] D.W. Woodruff, J.W. Westwater, Steam condensation on various gold surfaces, *J. Heat Trans.* 103 (1981) 685–692.
- [7] A. Daniel, F. Christophe, A.R. Betz, T.M. Schutzius, G. Ranjan, D. Arindam, C. Kim, C.M. Megaridis, Surface engineering for phase change heat transfer: a review, *MRS Energy Sustain.* 1 (2014) E4.
- [8] S. Kim, K.J. Kim, Dropwise condensation modeling suitable for superhydrophobic surfaces, *J. Heat Trans.* 133 (2011) 081502.
- [9] J. Xie, J. Xu, Q. Liu, X. Li, Coupling diffusion welding technique and mesh screen creates heterogeneous metal surface for droplets array, *Adv. Mater. Interfaces* 4 (2017) 1700684.
- [10] N. Miljkovic, R. Enright, Y. Nam, K. Lopez, N. Dou, J. Sack, E.N. Wang, Jumping droplet-enhanced condensation on scalable superhydrophobic nanostructured surfaces, *Nano Lett.* 13 (2013) 179–187.
- [11] H. Hu, G. Tang, D. Niu, Experimental investigation of condensation heat transfer on hybrid wettability finned tube with large amount of noncondensable gas, *Int. J. Heat Mass Transf.* 85 (2015) 513–523.
- [12] L. Zhong, X. Ma, S. Wang, M. Wang, X. Li, Effects of surface free energy and nanostructures on dropwise condensation, *Chem. Eng. J.* 156 (2010) 546–552.
- [13] J. Xie, J. Xu, W. Shang, K. Zhang, Dropwise condensation on superhydrophobic nanostructure surface, part II: Mathematical model, *Int. J. Heat Mass Transf.* 127 (2018) 1170–1187.
- [14] D. Torresin, M.K. Tiwari, C.D. Del, D. Poulikakos, Flow condensation on copper-based nanotextured superhydrophobic surfaces, *Langmuir* 29 (2013) 840–848.
- [15] N. Watanabe, M. Aritomi, A. Machida, Time-series characteristics and geometric structures of drop-size distribution density in dropwise condensation, *Int. J. Heat Mass Transf.* 76 (2014) 467–483.
- [16] K.K. Varanasi, M. Hsu, N. Bhat, W. Yang, T. Deng, Spatial control in the heterogeneous nucleation of water, *Appl. Phys. Lett.* 95 (2009) 144101.
- [17] M. He, Q. Zhang, X. Zeng, D. Cui, J. Chen, H. Li, J. Wang, Y. Song, Hierarchical porous surface for efficiently controlling microdroplets' self-removal, *Adv. Mater.* 25 (2013) 2291–2295.
- [18] L. Mishchenko, M. Khan, J. Aizenberg, B.D. Hatton, Spatial control of condensation and freezing on superhydrophobic surfaces with hydrophilic patches, *Adv. Funct. Mater.* 23 (2013) 4577–4584.

- [19] A. Chatterjee, M.M. Derby, Y. Peles, M.K. Jensen, Enhancement of condensation heat transfer with patterned surfaces, *Int. J. Heat Mass Transf.* 71 (2014) 675–681.
- [20] C.W. Yao, J.L. Alvarado, C.P. Marsh, B.G. Jones, M.K. Collins, Wetting behavior on hybrid surfaces with hydrophobic and hydrophilic properties, *Appl. Surf. Sci.* 290 (2014) 59–65.
- [21] Y. Hou, M. Yu, X. Chen, Z. Wang, S. Yao, Recurrent filmwise and dropwise condensation on a beetle mimetic surface, *ACS Nano* 9 (2015) 71–81.
- [22] B. Mondal, G.E.M. Mac, Q. Xu, V.M. Egan, J. Punch, A.M. Lyons, Design and fabrication of a hybrid superhydrophobic-hydrophilic surface that exhibits stable dropwise condensation, *ACS Appl. Mater. Inter.* 7 (2015) 23575–23588.
- [23] J.B. Boreyko, R.R. Hansen, K.R. Murphy, S. Nath, S.T. Retterer, C.P. Collier, Controlling condensation and frost growth with chemical micropatterns, *Sci. Rep.* 6 (2016) 19131.
- [24] I.H. Kim, H.C. No, Physical model development and optimal design of PCHE for intermediate heat exchangers in HTGRs, *Nucl. Eng. Des.* 243 (2012) 243–250.
- [25] J. Xu, X. Yu, W. Jin, Porous-wall microchannels generate high frequency “eye-blinking” interface oscillation, yielding ultra-stable wall temperatures, *Int. J. Heat Mass Transf.* 101 (2016) 341–353.
- [26] J. Xie, J.L. Xu, X. Li, H. Liu, Dropwise condensation on superhydrophobic nanostructure surface, Part I: Long-term operation and nanostructure failure, *Int. J. Heat Mass Transf.* 129 (2019) 86–95.
- [27] X. Chen, M.M. Derby, Combined visualization and heat transfer measurements for steam flow condensation in hydrophilic and hydrophobic mini-gaps, *J. Heat Trans.* 138 (9) (2016) 091503.
- [28] C. Fang, J.E. Steinbrenner, F.M. Wang, K.E. Goodson, Impact of wall hydrophobicity on condensation flow and heat transfer in silicon microchannels, *J. Micromech. Microeng.* 20 (4) (2010) 045018.
- [29] M.M. Derby, A. Chatterjee, Y. Peles, M.K. Jensen, Flow condensation heat transfer enhancement in a mini-channel with hydrophobic and hydrophilic patterns, *Int. J. Heat Mass Transf.* 68 (2014) 151–160.
- [30] G. Wypych, *Handbook of Polymers*, Chemtech Publishing, Toronto, ON, 2012, pp. 556–570.
- [31] X. Yu, J. Xu, J. Yuan, W. Zhang, Microscale phase separation condensers with varied cross sections of each fluid phase: Heat transfer enhancement and pressure drop reduction, *Int. J. Heat Mass Transf.* 118 (2018) 439–454.
- [32] S.M. Kim, I. Mudawar, Universal approach to predicting heat transfer coefficient for condensing mini/micro-channel flow, *Int. J. Heat Mass Transf.* 56 (2013) 238–250.
- [33] V.P. Carey, *Liquid-vapor phase-change phenomena*, 2nd Edition., CRC Press, 2007.
- [34] I.O. Ucar, H.Y. Erbil, Dropwise condensation rate of water breath figures on polymer surfaces having similar surface free energies, *Appl. Surf. Sci.* 259 (2012) 515–523.
- [35] S. Daniel, M.K. Chaudhury, J.C. Chen, Fast Drop Movements Resulting from the Phase Change on a Gradient Surface, *Science* 291 (2001) 633–636.
- [36] F. Brochard, Motions of droplets on solid surfaces induced by chemical or thermal gradients, *Langmuir* 5 (1989) 432–438.
- [37] J. Xie, J. Xu, X. He, Q. Liu, Large scale generation of micro-droplet array by vapor condensation on mesh screen piece, *Sci. Rep.* 7 (2017) 39932.
- [38] T.Q. Liu, W. Sun, X.Q. Li, X.Y. Sun, H.R. Ai, Growth modes of condensates on nanotextured surfaces and mechanism of partially wetted droplet formation, *Soft Matter* 9 (41) (2006) 9807–9815.
- [39] J.B. Boreyko, C.H. Chen, Self-Propelled dropwise condensate on superhydrophobic surfaces, *Phys. Rev. Lett.* 103 (2009) 184501.
- [40] D. Richard, D. Quere, Viscous drops rolling on a tilted non-wettable solid, *Europhys. Lett.* 48 (1999) 286–291.